Hindawi
Advances in Materials Science and Engineering
Volume 2019, Article ID 6320601, 11 pages
https://doi.org/10.1155/2019/6320601

Research Article

Attenuation Characteristics of Stress Wave Peak in Sandstone Subjected to Different Axial Stresses

Yun Cheng[1], **Zhanping Song**[1,2], **Jiefang Jin**[3], **and Tengtian Yang**[2,4]

[1]*School of Civil Engineering, Xi'an University of Architecture and Technology, Xi'an 710055, China*
[2]*Shaanxi Key Laboratory of Geotechnical and Underground Space Engineering, Xi'an 710055, China*
[3]*School of Architectural and Surveying Engineering, Jiangxi University of Science and Technology, Ganzhou 341000, China*
[4]*China Railway Bridge Engineering Bureau Group Co. Ltd., Tianjin 300300, China*

Correspondence should be addressed to Yun Cheng; chengyun_ifu@163.com and Zhanping Song; songzhpyt@xauat.edu.cn

Received 8 March 2019; Revised 3 June 2019; Accepted 18 June 2019; Published 3 July 2019

Academic Editor: Fernando Lusquiños

To investigate the effect of axial stress on the attenuation characteristics of stress wave peaks, stress wave propagation experiments with small disturbance of a sandstone bar were carried out by a modified split Hopkinson pressure bar test system. Then, effects of axial stress on the waveform, attenuation rate, temporal-spatial attenuation characteristics, and attenuation sensitivity factor of the peak were studied. The results showed that the presence or absence of axial stress has a significant effect on the waveform. With axial stress loading, both temporal and spatial attenuation rates undergo similar development stages, "nonlinear stage + linear stage," in which the demarcation stress (σ/σ_c) is 30%. Under the same axial stress, the peak decreases exponentially with the propagation time and distance with different attenuation intensities. With increasing axial stress, the temporal and spatial response intensities also experience "nonlinear stage + linear stage." However, the temporal and spatial attenuation coefficients undergo three stages, first a dramatic decrease, then gentle development, and finally a sharp increase, in which demarcation stresses (σ/σ_c) are 30% and 55%. The defined attenuation sensitivity factor can well describe the attenuation sensitivity of peaks to different axial stresses. The conclusions can provide a theoretical reference for rock mass stability analysis in blasting excavation.

1. Introduction

Stress wave motion in the rock mass is a fundamental physical phenomenon, which has a wide range of applications in the development of underground rock mass engineering, such as tunnel excavation and mining [1–3]. Therefore, rock mass instability caused by natural or human activities is studied, such as earthquakes, excavations, and mining vibrations, and this not only destroys the stress balance of original rock but also leads to the phenomenon of stress redistribution [1], thus causing the changes of the physical and mechanical properties. Take the loading and unloading processes of rock stress as an example, and there will be pores evolution such as the closure of primary pores and the initiation and expansion of new pores, resulting in different damage degrees of the rock mass [4–7]. However, the rock mass instability induced by those natural and human activities is closely related to stress wave propagation. For all this, it is of significance to study the propagation and attenuation characteristics of stress waves in a rock mass with different static stress conditions for the construction and operation safety of rock mass engineering.

Currently, given the blasting excavation of deep engineering rock mass, the research focus can be divided into dynamic response problems [4, 6, 8, 9] and stress wave propagation problems [10–12]. However, since the complexity and discontinuity of the rock mass, the propagation and attenuation characteristics of stress waves are also very complicated, so there is no unified quantitative relationship to describe those attenuation mechanisms [4]. Engineering practice has shown that the change in original rock stress is calculated in milliseconds [13]; this indicates the necessity to study the dynamic response problem during the rock mass excavation. Thus, to meet the engineering needs, the impact

damage, deformation and failure characteristics, and energy dissipation mechanism of the rock mass have been studied theoretically and practically, and the relevant theories and numerical models have been established [6, 14, 15].

Meanwhile, to explore the stress wave propagation and attenuation characteristics, Aliabadian et al. [9] discussed the deformation and fracture behaviors of rock specimens under impact loads in conjunction with optical emission that accompanies the fracture and analyzed the waveforms of the incident, reflected, and transmitted strain pulse. Ju et al. [16] presented the property of stress wave propagation in jointed rocks using the split Hopkinson pressure bar (SHPB) technique and analyzed the influence of the rough joint surface configuration on stress waves. Li et al. [17] found that the impact velocity, contact area ratio, and relative intensity degree of a joint surface area affected the dynamic stress-strain relation of rock masses, stress wave propagation, and the transmission coefficient of the stress wave. By using the theory of wave mechanics and improved SHPB, Liu et al. [18] and Guo and Wei [19] analyzed the influence of stress wave amplification and static loading on the waveform, transmission coefficient, reflection coefficient, and energy dissipation in a coal rock mass. Thus, it can find that the stress wave propagation and attenuation characteristics in a rock mass are related not only to elastic parameters and static stress but also to the distribution of microcracks.

Furthermore, the physical, mechanical, and structural characteristics of the rock mass can be deduced by investigating the attenuation law of the stress wave. These studies indicate that some beneficial results have been achieved for the static stress affecting the dynamic mechanical response of rock; however, there are few studies on the effect of stress wave propagation characteristics on a rock mass with different static stresses. Besides, although the rock specimen with a small length : diameter ratio (less than 1) is representative [20], the attenuation characteristics of the stress wave in whole deformed rock cannot be obtained, while the rock with a more significant length : diameter ratio can achieve the expected effect by setting multiple test points measuring several multidata of stress wave signals simultaneously.

In this study, we aim at discussing the attenuation characteristics of stress wave peaks in sandstone under different axial stresses. Because of the need to simultaneously obtain multiple sets of experimental data, we first design a sandstone bar with a length-diameter ratio of 65 through exploratory tests and gradually load 13 different axial stresses on it by a modified split Hopkinson pressure bar (SHPB) test system. Then, impact experiments with small disturbance are conducted on the specimen by fixing the impact velocity of the striker bar, and the stress wave signals with different axial stresses are obtained. The experimental data are analyzed from the viewpoints of (a) stress wave characteristics, (b) the variation law of attenuation rates of wave peaks, (c) temporal-spatial attenuation characteristics of stress wave peaks, and (d) pore evolution characteristics of specimens with increasing of axial stress, and empirical mathematical models are established based on experimental results. The research conclusions provide the theoretical basis for the stability analysis of rock mass engineering such as blasting and excavation.

2. Experiment and Data Acquisition Procedures

2.1. Experimental Apparatus. The modified split Hopkinson pressure bar (SHPB) test system in the impact mechanics laboratory of Jiangxi University of Science and Technology can provide both axial stress and stress wave, as shown in Figure 1. This test system consists of a stress loading device, dynamic loading device, laser velocimeter device (JXCS-02), data acquisition device (SDY2017A dynamic strain meter), and data display device (Yokowaga DL850E oscillograph). The spindle striker bar in the chamber of the dynamic loading device can load a half-sine wave and eliminate Pochhammer-Chree (PC) oscillation [12]. The specific dimensions of the striker bar are also shown in Figure 1(a). The sampling time ranges from $-100\,\mu$s to $900\,\mu$s, the interval is 1 μs, and it can collect 1000 time points.

2.2. Experimental Material

2.2.1. Uniaxial Compressive Strength (σ_c) of Sandstone. The sandstone used in the dynamic test is taken from the Huaping quarry in Ganzhou, Jiangxi Province, China. The sandstone is red, and it has good integrity and homogeneity. The density, particle size, and original porosity of the sandstone are 2.35 g/cm^3, 0.05~2.00 mm, 5.22%, respectively. The stress-strain curve of the sandstone (Φ50 mm × 100 mm) is tested by using RMT-150C rock mechanical test machine developed by Institute of Rock and Soil Mechanics, Chinese Academy of Sciences, as shown in Figure 2, indicating that the failure process experiences the compaction stage (OP)—elastic deformation stage (PQ)—cracks development and expansion stage (QM)—failure stage (MN). The uniaxial compressive strength (σ_c) and elastic modulus (E) are 52.00 MPa and 5.65 GPa, respectively.

2.2.2. Specimen Preparation for the Dynamic Test. Two factors should be considered when designing the specimen: (a) due to the attenuation characteristics of stress wave peaks in sandstone under different axial stresses, the sandstone specimen can be arranged with multiple signal points to measure sets of data, that is, considering the larger length-diameter ratio; (b) considering the brittle failure characteristic under axial stress loading. After exploration tests, the specimen is processed into a sandstone bar with a section of 80 mm × 80 mm and a length of 1500 mm. The tentative experimental results show that the compressive strength (the critical stress of instability) of the specimen for the dynamic test is about 39.00 MPa.

Besides, the procedures of the exploration test are as follows: The sandstone bar is fixed between the incident bar and the transmission bar, and the axial stress is loaded by the stress loading device according to the test scheme (shown in Figure 3). Three small disturbance impact tests are carried out under each axial stress. The sandstone bar is destroyed when the axial stress is loaded to 39 MPa; that is, 39 MPa is the critical stress of instability.

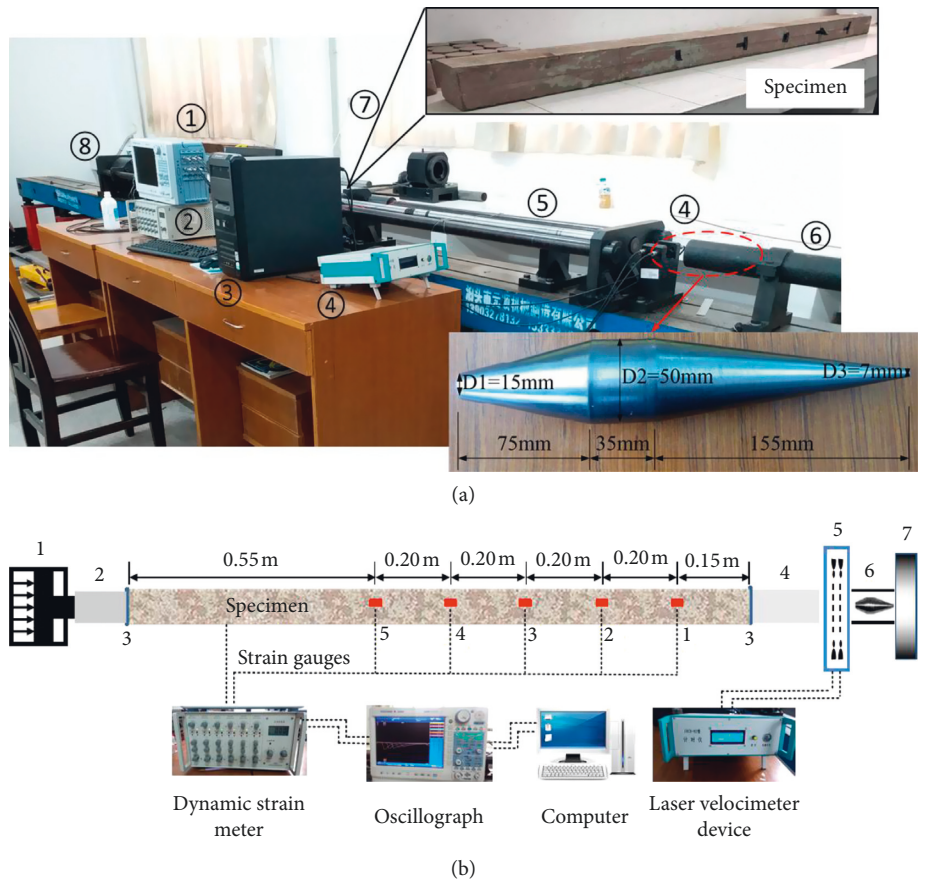

Figure 1: (a) Experimental apparatus: ① oscillograph; ② dynamic strain meter; ③ computer; ④ laser velocimeter device; ⑤ incident bar; ⑥ chamber of striker bar; ⑦ specimen; ⑧ stress loading device. (b) Diagram of the modified split Hopkinson pressure bar (SHPB) system: 1. stress loading device; 2. transmission bar; 3. steel pads; 4. incident bar; 5. laser velocimeter; 6. striker bar; 7. high-pressure air chamber.

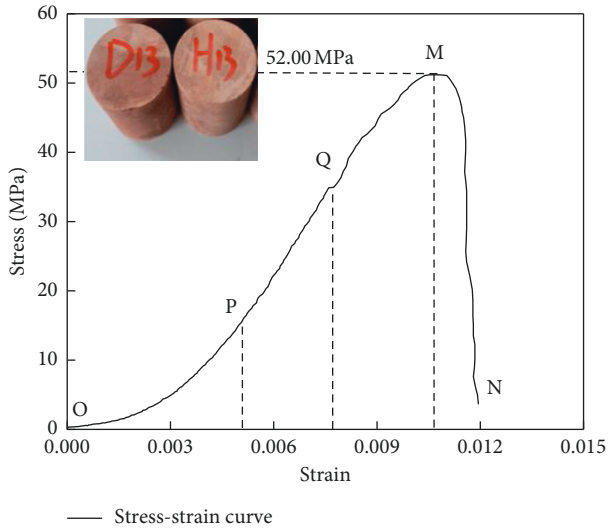

Figure 2: Stress-strain curve of sandstone.

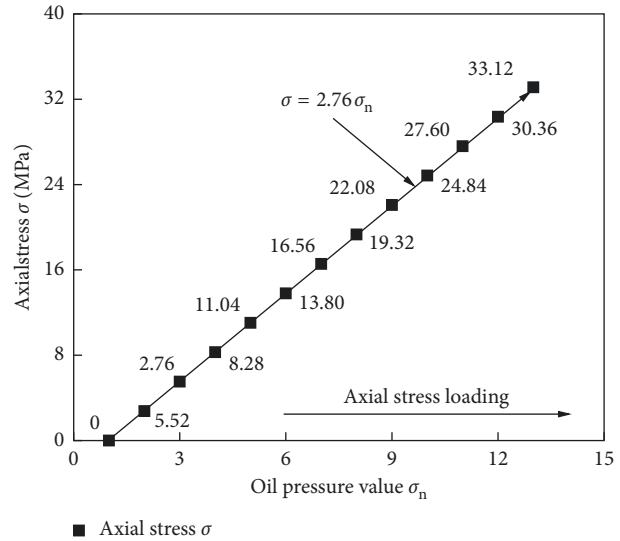

Figure 3: Axial stress of the specimen.

2.3. Empirical Principle. The axial stress loading range and impact velocity of the striker bar (that is, stress wave strength) should be considered in the tests. The specific test principle is as follows:

(1) Since the hydraulic pump loads the axial stress of the specimen, its values (σ_n) are set at 0, 1, 2, 3, . . ., and 12 MPa. Then, the axial stress (σ) of the specimen can be obtained according to equation (1), and S_1/

$S_2 \approx 2.76$ is the cross-sectional area ratio of the hydraulic pump piston to the specimen; the axial stress (σ) is shown in Figure 3:

$$\sigma = 2.76\sigma_n. \quad (1)$$

(2) The previous study has shown that when stress wave amplitude is less than 60% of rock static strength under repeated stress waves, the damage caused by the cyclic stress wave could be ignored [21]. Based on this, the cyclic stress wave amplitude in the test is confirmed through explorative tests to minimize the damage. To achieve this effect, the striker bar struck the incident bar at a velocity of about 4.38 m/s and the stress wave is a kind of half-sine wave. The impact velocity is measured by using a laser velocimeter.

(3) After steps (1) and (2), the specimen is assembled with the SHPB test system, and the steel pads with the area slightly larger than the cross section of the specimen are added to the interfaces between the specimen and the incident bar (transmission bar) to prevent the occurrence of stress concentration phenomenon. Besides, coupling agents (mechanical butter) are smeared on both sides of the steel pads to reduce the interfacial friction to ensure the excellent transmission of stress wave signals.

(4) Arrange the test points on the surface of the specimen. There are 5 test points on the surface of the specimen, which are test points A, B, C, D, and E. Two longitudinally symmetric strain gauges (its resistance value, size, supply voltage, sensitivity coefficient, and strain limit are $120 \pm 1\,\Omega$, $8\,\text{mm} \times 5\,\text{mm}$, 3~10 V, ±2.0% and 20000 μm/m, respectively) are attached to each test point to lower the test error. Figure 1 shows the locations and spacings of the test points.

(5) Three impact tests of the same strength under each axial stress are carried out, and then the stress wave signals with different axial stresses are saved. The propagation path of the stress wave is the incident end of specimen ⟶ strain gauge ⟶ dynamic strain gauge ⟶ oscilloscope ⟶ computer. Repeat all stress wave tests in this way.

3. Results and Discussion

3.1. Waveform Characteristics of Stress Wave. Due to a large number of experimental data, only the waveforms of 0 MPa, 8.28 MPa, 16.56 MPa, 24.84 MPa, and 33.13 MPa are shown in Figure 4. The stress wave amplitudes are characterized by the measured voltage values (mV), and the positive and negative ordinate values indicate the tensile wave and compression wave, respectively. Taking Figure 4(e) as an example, with increasing of propagation time, the stress wave first "jumps" along the negative direction of the longitudinal axis to reach the stress wave peak (hereinafter referred to as peak), denoted as P_n (mV), and then the stress wave continues to "climb" to form a tensile wave.

Simultaneously, in order to show the variation characteristics of the peak, the peak and its corresponding time (denoted as P_n/t_n, where n is A, B, C, D, and E) at each test point under different axial stresses are extracted from the stress waves in Figure 4, as shown in Table 1. The working condition of 0.1863/142 shown in Table 1 is a good example, denoting that the peak and its corresponding time tested at test point A ($\sigma = 0$ MPa) is $P_n = 0.1863$ mV and $t_n = 142\,\mu$s, respectively.

The following observations can be made from Figure 4 and Table 1 for all the tested stress waves:

(1) When the specimen has specific axial stress, there is no apparent difference in the waveform for all test points, except that the peak shows the attenuation trend with increasing of the propagation distance of stress waves.

(2) According to Figure 4(a) and Figures 4(b)–4(e), the presence or absence of axial stress in the specimen has a remarkable influence on the waveform and the propagation of stress wave. First, no tensile wave occurs at any test point when there is no axial stress (see Figure 4(a)). Second, the tensile wave appears in the tail of the stress wave at each test point and increases with increasing of axial stress (see Figures 4(b)–4(e)). Third, the peaks at the same test point will decrease gradually with increasing of axial stress (see Table 1).

(3) With increasing of axial stress, the stress wave gradually shows a "double peaks" characteristic, that is, the compression wave peak and the tensile wave peak exist simultaneously (the analysis of "double peaks" characteristics will be presented in the next study), which shows that the existence of axial stress has a significant effect on the formed tensile wave. The reason is that the increased axial stress affects the porosity evolution, such as the closure of primary pores, the initiation, and expansion of new pores, thus resulting in different damage degrees and changing the transmission and reflection capacity of the specimen [4, 18].

3.2. Effect of Axial Stress on Attenuation Rate of Peak. As mentioned above, the natural rock mass has an anisotropic characteristic and complex structure. Therefore, the transmission and reflection phenomenon will occur when the stress wave propagates to the crack and structure surface, and this will not only results in the transformation of compression wave to tensile wave but also causes the attenuation of stress wave in propagation time and propagation distance. To show the difference in the attenuation rate in propagation time and propagation distance, we define the temporal attenuation rate V_t (mV/μs) as the ratio of the difference value of $P_A - P_E$ to the difference value of $t_E - t_A$, and define the spatial attenuation rate V_x (mV/m) as the ratio of the difference value of $P_A - P_E$ to the difference value of $x_E - x_A$, as follows:

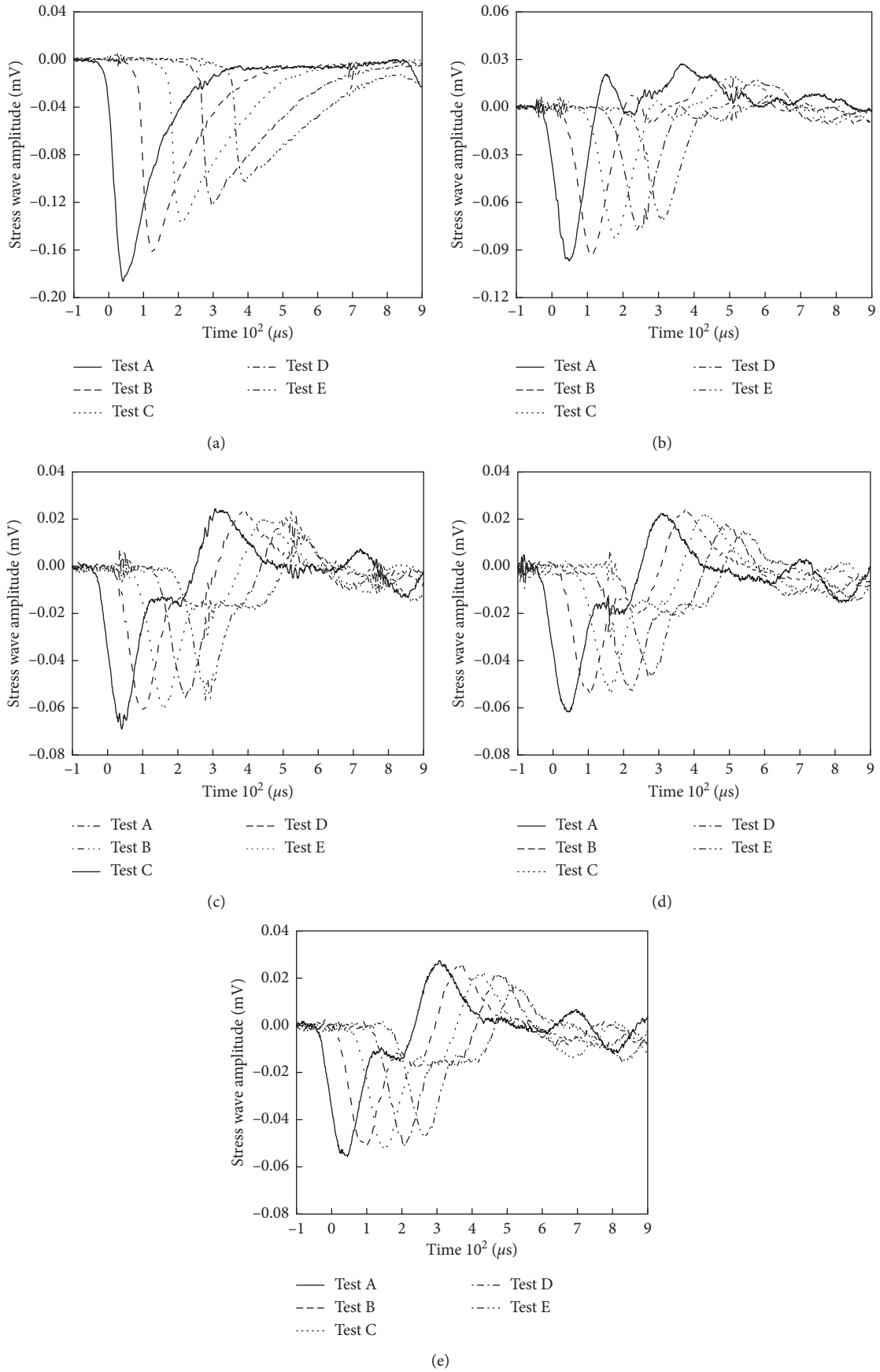

Figure 4: Waveforms under different axial stresses. (a) 0 MPa. (b) 8.28 MPa. (c) 16.56 MPa. (d) 24.84 MPa. (e) 33.12 MPa.

Table 1: Peak and its corresponding time under different axial stresses.

Axial stress (MPa)	Peak (mV)/corresponding time (μs)					Impact velocity (m/s)
	Test point A	Test point B	Test point C	Test point D	Test point E	
0.00	0.1863/142	0.1620/227	0.1377/311	0.1230/398	0.1033/494	4.45
2.76	0.1543/155	0.1403/218	0.1200/299	0.1073/372	0.0900/452	4.44
5.52	0.1247/152	0.1173/214	0.1037/289	0.0943/356	0.0830/429	4.47
8.28	0.0967/148	0.0940/210	0.0823/276	0.0787/341	0.0717/413	4.46
11.04	0.0807/141	0.0790/212	0.0710/266	0.0680/334	0.0643/398	4.35
13.80	0.0727/142	0.0693/202	0.0633/266	0.0617/323	0.0593/393	4.38
16.56	0.0660/142	0.0613/209	0.0573/261	0.0553/330	0.0527/378	4.39
19.32	0.0653/142	0.0577/201	0.0553/257	0.0547/327	0.0523/378	4.41
22.08	0.0630/137	0.0570/199	0.0567/259	0.0543/314	0.0497/374	4.36
24.84	0.0617/140	0.0540/202	0.0547/263	0.0530/322	0.0463/372	4.45
27.60	0.0597/149	0.0553/192	0.0520/252	0.0510/316	0.0480/379	4.49
30.36	0.0593/149	0.0550/204	0.0520/261	0.0480/318	0.0460/382	4.43
33.12	0.0587/131	0.0537/197	0.0493/250	0.0490/319	0.0437/380	4.47

$$V_t = \frac{P_A - P_E}{t_E - t_A}, \tag{2}$$

$$V_x = \frac{P_A - P_E}{x_E - x_A}, \tag{3}$$

where t_E and t_A denote the corresponding times of peak P_E and peak P_A and x_E and x_A mean the corresponding locations of test point E and test point A.

Studies show the relationships between the temporal and spatial attenuation rates V_t and V_x under different axial stresses calculated by equations (2) and (3), shown in Figure 5.

The following conclusions can be drawn from Figure 5:

(1) As the axial stress of specimen increases, both temporal and spatial attenuation rates V_t and V_x show a similar tendency and can be divided into two stages, "nonlinear stage + linear stage." When the axial stress is lower than 16.56 MPa, both temporal and spatial attenuation rates V_t and V_x decrease sharply and exponentially with axial stress, reduced by 76.09% and 83.97%, respectively. When the axial stress exceeds 16.56 MPa, the two curves gradually become smooth and slow, approximately linear, and then converge at 5.0×10^{-5} mV/μs and 2.0×10^{-5} mV/m, respectively. These indicate that the temporal and spatial attenuation rates have different sensitivity to different axial stress levels. The reason is that with the axial stress loading, the energy absorption of the stress wave reduces due to the decreased porosity of the specimen. If the demarcation point of axial stress of the two stages is expressed as the ratio of axial stress (σ) of the specimen to uniaxial compressive strength (σ_c) of sandstone, both of which are about $\sigma/\sigma_c = 30\%$.

(2) Although the values of V_t and V_x have a similar development tendency with increasing of axial stress, V_t is always larger than V_x. Regression analysis shows that both V_t, V_x and axial stress have the exponential relationships; however, with increasing of axial stress, the attenuation coefficient of V_t (0.09) is smaller than that of V_x (0.13), which indicates that the attenuation sensitivity of V_x in propagation distance is greater than that in propagation time. Regression relations between V_t, V_x and axial stress are given in equations (4) and (5), respectively:

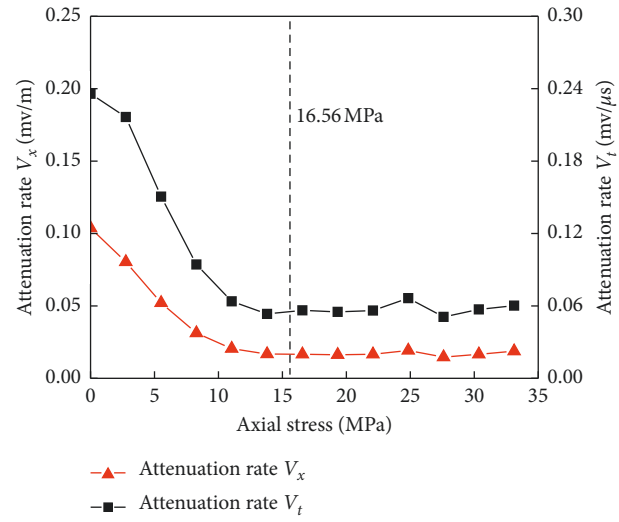

Figure 5: Relationships between temporal and spatial attenuation rates of peak and axial stress.

$$V_t = 0.3469e^{(-\sigma/11.05)} + 0.0043\sigma - 0.0945\left(R^2 = 0.9402\right), \tag{4}$$

$$V_x = 0.1234e^{(-\sigma/7.75)} + 0.0011\sigma - 0.0160\left(R^2 = 0.9262\right), \tag{5}$$

where the applicable conditions of equations (4) and (5) are $0\,\text{MPa} \le \sigma \le 33.12\,\text{MPa}$ and the impact velocity of the striker bar is 4.43 m/s.

3.3. Analysis of Temporal-Spatial Attenuation Characteristics of Peak

3.3.1. Theoretical Analysis and Deduction of Attenuation Parameters. Table 1 shows that the peak decreases gradually with increasing of propagation time and propagation

distance when the specimen has certain axial stress, and the peak at the same test point also decreases with increasing of axial stress. And for this, the attenuation characteristics of the peak in propagation time and propagation distance under different axial stresses in this section will be discussed. If the attenuation degree of the peak with increasing of propagation time is expressed by the temporal attenuation coefficient (α_t), the relative variation of the peak when the stress wave propagates from t to $t + \Delta t$ can be expressed as

$$\frac{P(t + \Delta t) - P(\Delta t)}{P(t)} = -\alpha_t \Delta t, \tag{6}$$

where $P(t)$ and $P(t + \Delta t)$ denote the peaks at time t and time $t + \Delta t$, respectively. It is clear that, from equation (6), the relative variation of the peak is proportional to Δt, and the proportional coefficient ($-\alpha_t$) represents the temporal attenuation of stress wave. If $\Delta t \longrightarrow 0$, equation (6) can be written as follows:

$$\frac{dP(t)}{dt} = -\alpha_t P(t). \tag{7}$$

Solving the differential equation (7), the temporal attenuation function $P(t)$ of the peak is expressed as

$$P(t) = \beta_t e^{-\alpha_t t}, \tag{8}$$

where β_t denotes the temporal response amplitude (mV) of the peak at the incident end of the specimen with the same impact velocity, defined as the temporal response intensity. α_t denotes the temporal attenuation coefficient (μs^{-1}) of the peak. Equation (8) shows that the peak decays exponentially with increasing of propagation time, and the attenuation intensity depends on the attenuation coefficient α_t.

Meanwhile, according to the similar analysis of spatial attenuation characteristics of the peak, the spatial attenuation function $P(x)$ can be expressed as

$$P(x) = \beta_x e^{-\alpha_x x}, \tag{9}$$

where β_x denotes the spatial response amplitude (mV) of the peak at the incident end of the specimen under the same impact velocity, having the same physical dimension with β_t, defined as the spatial response intensity. α_x denotes the spatial attenuation coefficient (m^{-1}) of the peak, which can define the attenuation intensity in propagation distance. However, the spatial attenuation coefficient has a different physical dimension compared with the temporal attenuation coefficient in equation (8).

Based on above theoretical analysis, the regression analysis is performed on the data given in Table 1 by equations (8) and (9), and then we obtain the temporal and spatial response intensities and temporal and spatial attenuation coefficients of the specimen with different axial stresses, summarized in Table 2.

3.3.2. Effect of Axial Stress on Temporal-Spatial Response Intensities of Peak. Figure 6 shows the relationships between temporal and spatial response intensities of the peak and axial stress. As can be seen from Figure 6 and Table 2 that with the increase of axial stress, the temporal and spatial response intensities of the peak show a similar attenuation tendency with different attenuation degrees, that is, the development trend of "nonlinear stage + linear stage."

At the first stage, the primary pores of the specimen gradually closed because of the axial stress loading, which causes the porosity reduction, thus leading the attenuation intensity to decrease slowly. When the axial stress increases from 0 MPa to 16.56 MPa, the temporal response intensity decreases from 0.2352 mV to 0.0746 mV with a 68.28% attenuation, and the spatial response intensity of the peak decreases from 0.2081 mV to 0.068 mV, which is reduced by 67.32%. Regression analysis manifests that the spatial and temporal response intensities decay exponentially with increasing of axial stress in the nonlinear stage. At the second stage, when the axial stress is more than 16.56 MPa, the temporal and spatial response intensities are gradually converged at 0.0700 mV and 0.0620 mV, respectively, showing the relative linear attenuation with increasing of axial stress. This reason is that with the gradual compression of the specimen at this stage, the porosity gradually reaches the stable phase, and the absorption degree of stress wave energy is reduced [22]. Comprehensive analysis shows that axial stress boundary points of the nonlinear stage and linear stage roughly coincide with that in Figure 5, which is $\sigma/\sigma_c = 30\%$.

In addition, Table 2 also indicates that the temporal and spatial response intensities are approximately equal under different axial stresses, and the ratio β_x/β_t is between 0.85 and 0.94. It is not an accident for the phenomenon as mentioned above, which is consistent with the physical characteristic of the same dimension of spatial and temporal response intensities. Meanwhile, the attenuation characteristic of spatial response intensity has consistency with that of temporal response intensity [23]. Regression analysis shows that β_x/β_t has a proper exponential function with axial stress, as shown in Figure 7.

3.3.3. Effect of Axial Stress on Temporal-Spatial Attenuation Coefficients of Peak. Comparison of the values of temporal and spatial response intensities given in Table 2 shows a significant difference with increasing of axial stress.

Figure 8 shows the relationships between temporal and spatial attenuation coefficients and axial stress of the specimen. It can be seen that the axial stress has a remarkable influence on the temporal and spatial attenuation coefficients. With increasing of axial stress, the temporal and spatial attenuation coefficients undergo three development stages with different variation degrees: first a dramatic decrease, then gentle development, and finally a sharp increase. The demarcation points of axial stress in the three stages are roughly $\sigma/\sigma_c = 30\%$ and $\sigma/\sigma_c = 55\%$. In the first stage, when the stress ratio σ/σ_c is less than 30%, the porosity of the specimen will decrease with increasing of axial stress, causing the dramatic decrease of the temporal and spatial attenuation coefficients. The reason is that the primary pores in the specimen are compacted, and then the energy dissipation rate of the stress wave is reduced. This stage can be called the stress strengthening stage. In the second stage,

Table 2: Temporal-spatial response intensities and attenuation coefficients.

Axial stress (MPa)	Temporal response intensity (mV)	Spatial response intensity (mV)	Temporal attenuation coefficient (μs^{-1})	Spatial attenuation coefficient (m^{-1})
0.00	0.2352	0.2081	0.0019	0.7273
2.76	0.2056	0.1741	0.0018	0.6733
5.52	0.1588	0.1374	0.0015	0.5159
8.28	0.1166	0.1042	0.0012	0.3883
11.04	0.0932	0.0854	0.0009	0.3012
13.80	0.0850	0.0751	0.0008	0.2613
16.56	0.0746	0.0680	0.0009	0.2771
19.32	0.0706	0.0652	0.0008	0.2486
22.08	0.0703	0.0646	0.0009	0.2618
24.84	0.0697	0.0632	0.0010	0.2952
27.60	0.0664	0.0623	0.0009	0.2822
30.36	0.0694	0.0619	0.0011	0.3226
33.12	0.0669	0.0611	0.0012	0.3408

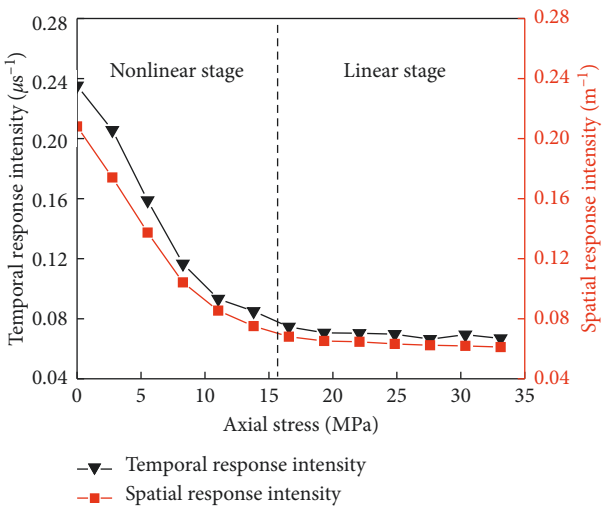

Figure 6: Relationships of temporal and spatial response intensities and axial stress.

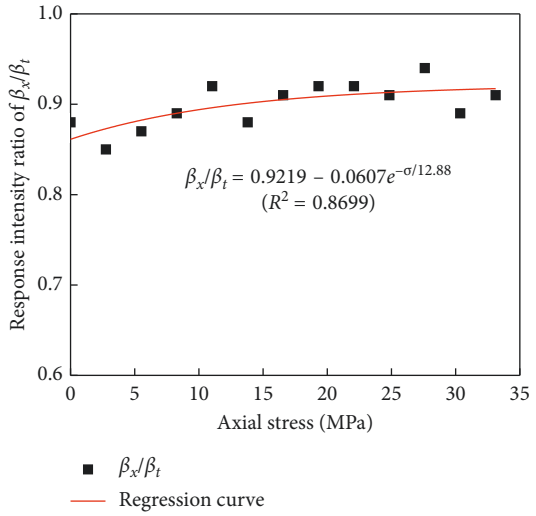

Figure 7: Relationship of response intensity ratio and axial stress.

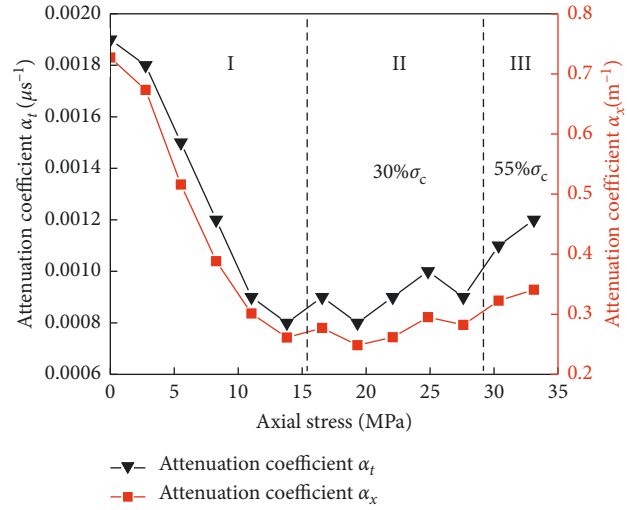

Figure 8: Relationships of temporal and spatial attenuation coefficients and axial stress.

when the stress ratio σ/σ_c is greater than 30% and less than 55%, the temporal and spatial attenuation coefficients of the peak show the gentle development with increasing of axial stress. The reason is the coexistence phenomenon of closed pores and newly formed pores caused by the loading stress of the specimen; however, when the number of closed pores is approximately equal to that of new ones, the porosity varies little. This stage is called the damage development stage. In the third stage, when the stress ratio σ/σ_c is greater than 50%, the number of newly formed pores will increase obviously and will be accompanied by the initiation and propagation of new microcracks, resulting in a sharp increase of internal damage degree. And then, the new pores and microcracks gradually dominate the evolution of porosity, thus causing a sharp increase in temporal and spatial attenuation coefficients with increasing axial stress. This stage is called the failure stage of the specimen.

Moreover, Table 2 shows that the regression values of temporal and spatial attenuation coefficients are differed by 2~3 orders of magnitude, although they present the same

development tendency as shown in Figure 8. The reason is that there are different dimensions for temporal and spatial attenuation coefficients. Therefore, the stress waves have consistency in temporal and spatial attenuation, and the different data also illustrate the different sensitivities to various axial stress stages that are subjected to the specimen. Furthermore, equations (10) and (11) also give the regression lines of the quadratic function of spatial and temporal attenuation coefficients:

$$\alpha_x = 1.08 \times 10^{-3}\sigma^2 - 4.66 \times 10^{-2}\sigma + 0.74\left(R^2 = 0.9462\right), \tag{10}$$

$$\alpha_t = 2.47 \times 10^{-6}\sigma^3 - 1.04 \times 10^{-4}\sigma + 1.92 \times 10^{-3}\left(R^2 = 0.9088\right), \tag{11}$$

where the applicable conditions of equations (4) and (5) are $0\ \text{MPa} \le \sigma \le 33.12\ \text{MPa}$ and the impact velocity of the striker bar is 4.43 m/s.

3.4. Analysis of Attenuation Sensitivity Factor. Rock is a natural damage material, and it contains a large number of primary microcracks and new pores. When a rock mass is subjected to the natural and human activities, the stress redistribution phenomena will occur as a result of the external stress disturbance [8], thus causing the closure of primary pores and the initiation and expansion of new pores. However, the aforementioned evolution behavior of pores not only results in the changes of physical and mechanical properties, such as rock density and porosity, and but also alters the transmission ability of stress wave and the wave impedance of rock. Therefore, the porosity evolution is the main reason for further damage or failure of a rock material. It can be seen from the above analysis whether axial stress existing in the specimen has an obvious influence on the waveform, attenuation rate, and temporal-spatial attenuation characteristics. It also reflects the different sensitivity degrees of porosity to different axial stress ranges. Based on this finding, we introduce an attenuation sensitivity factor, which can be written as follows:

$$\chi = \frac{\alpha_x}{\alpha_t}. \tag{12}$$

Studies show that the introduced equation (12) can well calculate the attenuation sensitivity factor under different axial stresses, and its development tendency is shown in Figure 9. It is clear that with increasing axial stress, the attenuation sensitivity factor experiences the three stages: first a rapid decrease, then smooth development, and finally a sharp increase. The stress boundary points of the three stages are $\sigma/\sigma_c = 30\%$ and $\sigma/\sigma_c = 55\%$, which are consistent with those in Figure 8. It is due to the change in the attenuation sensitivity factor caused by the change in the wave impedance of sandstone [22]. In addition, the wave impedance can express as the product of stress wave velocity and sandstone density, which can measure the resistance of sandstone to the energy transmission of stress waves [24].

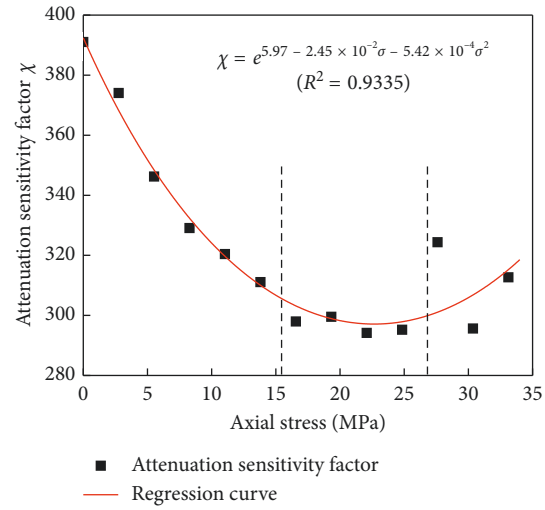

Figure 9: Relationship of attenuation sensitive factor and axial stress.

Therefore, we can infer that with increasing of axial stress, the wave impedance experiences three development stages, first a rapid increase, then smooth development, and finally a sharp decrease, and its variation tendency is opposite to the attenuation sensitivity factor. The reasons are that when the stress ratio σ/σ_c is less than 30%, the decreased porosity of sandstone results in the rapid increase of wave impedance and then reduces the attenuation sensitivity factor. When the stress ratio σ/σ_c is significantly more than 30% and less than 55%, the specimen porosity gradually reaches the stable condition, thus leading to the smooth development of the wave impedance and attenuation sensitivity factor. When the stress ratio σ/σ_c is more than 55%, as the axial stress continues to increase, the number of new pores increases rapidly and gradually dominates the development trend of the total pores in sandstone. Therefore, the reduced wave impedance exacerbates the increasing trend of the attenuation sensitivity factor.

4. Conclusions

Rock is a kind of porous geological material consisting of natural microholes and cracks whose closure degree affects the physical and mechanical properties. In this study, the modified split Hopkinson pressure bar (SHPB) test system is used to test the stress wave disturbance of the sandstone bar with the same impact strength. Then, the effects of axial stress on waveforms, attenuation rates, temporal-spatial attenuation characteristics, and attenuation sensitivity factors of stress wave peaks are studied, and then empirical models are established based on the experimental data. Conclusions obtained from the results of this study are summarized as follows:

(1) The impact tests under different axial stresses show that the presence or absence of axial stress in the specimen has a significant effect on the waveform of stress waves. The waveforms at various test points are approximately the same when axial stress is constant,

while the waveforms at the same test point vary greatly when axial stress changes, and the tensile waves appearing at the tail of stress waves are enlarged with increasing of axial stress.

(2) With increasing of axial stress, the decay tendencies of the temporal and spatial attenuation rates can be divided into two stages with different attenuation degrees, which are "nonlinear stage + linear stage." The demarcation points of axial stress in the two stages are $\sigma/\sigma_c = 30\%$. The temporal and spatial attenuation rates and axial stress have proper exponential functions; however, the attenuation degree of the spatial attenuation rate is higher than that of the temporal attenuation rate.

(3) Under the same axial stress, the peak decreases exponentially with the propagation time and propagation distance. With increasing of axial stress, both temporal and spatial response intensities experience the tendency of "nonlinear stage + linear stage", however, with different attenuation degrees. Besides, the temporal and spatial response intensities are approximately equal due to the same physical dimension of them.

(4) The axial stress has a significant influence on the temporal and spatial attenuation coefficients. With increasing of axial stress, the temporal and spatial attenuation coefficients undergo three stages, first a dramatic decrease, then gentle development, and finally a sharp increase. The demarcation points of axial stress roughly are $\sigma/\sigma_c = 30\%$ and $\sigma/\sigma_c = 55\%$. The main reasons are that the porosity and wave impedance are changed due to the axial stress loading. Also, the defined attenuation sensitivity factor can well describe the attenuation sensitivity of the peak to axial stress.

In this study, experiments related only to the sandstone material have been carried out due to the excellent porosity and secure processing of sandstone. The influence of rock types and rock cross-section shape on the attenuation characteristics of the peak will be the focus of future research work.

Data Availability

The data used to support the findings of this study are available from the corresponding author upon request.

Conflicts of Interest

The authors declare that they have no conflicts of interest.

Acknowledgments

The authors would like to thank the National Natural Science Foundation of China (Grant no. 51578447) and Fund of Housing Urban and Rural Construction Technology Research and Development Project Foundation of China(2017-K4-032).

References

[1] J.-H. Shin, H.-G. Moon, and S.-E. Chae, "Effect of blast-induced vibration on existing tunnels in soft rocks," *Tunnelling and Underground Space Technology*, vol. 26, no. 1, pp. 51–61, 2011.

[2] Y. W. Zhang, X. L. Weng, Z. P. Song et al., "Modeling of loess soaking induced impacts on metro tunnel using water soaking system in centrifuge," *Geofluids*, vol. 2019, Article ID 5487952, 17 pages, 2019.

[3] Z. P. Song, T. T. Yang, A. N. Jiang, D-F. Zhang, and Z-B. Jiang, "Experimental investigation and numerical simulation of surrounding rock creep for deep mining tunnels," *Journal of the Southern African Institute of Mining and Metallurgy*, vol. 116, no. 12, pp. 1181–1188, 2016.

[4] Ö. Aydan and H. Kumsar, "An experimental and theoretical approach on the modeling of sliding response of rock wedges under dynamic loading," *Rock Mechanics and Rock Engineering*, vol. 43, no. 6, pp. 821–830, 2010.

[5] Z. P. Song, S. H. Li, X. G. Zhang et al., "Study on strata settlement regular pattern induced by tunnel construction based on Peck formula," *Journal of Xian University of Architecture and Technology (Natural Science Edition)*, vol. 50, no. 2, pp. 190–195, 2018.

[6] S. Aziznejad, K. Esmaieli, J. Hadjigeorgiou, and D. Labrie, "Responses of jointed rock masses subjected to impact loading," *Journal of Rock Mechanics and Geotechnical Engineering*, vol. 10, no. 4, pp. 624–634, 2018.

[7] Z. Wang, J. Yao, N. Tian, J. Zheng, and P. Gao, "Mechanical behavior and damage evolution for granite subjected to cyclic loading," *Advances in Materials Science and Engineering*, vol. 2018, Article ID 4312494, 10 pages, 2018.

[8] F. Q. Gong, L. Zhang, X. B. Li et al., "Experimental study on fracture behaviors of hard rock under dynamic disturbance with different pre-static loads," *Chinese Journal of Rock Mechanics and Engineering*, vol. 36, no. 8, pp. 1841–1854, 2017.

[9] Z. Aliabadian, M. Sharafisafa, A. Mortazavi, and P. Maarefvand, "Wave and fracture propagation in continuum and faulted rock masses: distinct element modeling," *Arabian Journal of Geosciences*, vol. 7, no. 12, pp. 5021–5035, 2014.

[10] J. B. Wang, Z. Z. Ren, Z. P. Song et al., "Study of the effect of micro-pore characteristics and saturation degree on the longitudinal wave velocity of sandstone," *Arabian Journal of Geosciences*, vol. 12, no. 13, 2019.

[11] S. Mitrihani, "Numerical simulation of rock mass vibrations induced by nearby product," *Canadian Geotechnical Journal*, vol. 51, no. 11, pp. 1–10, 2014.

[12] Y. Cheng, Z. P. Song, J. F. Jin et al., "Variation of p-wave velocity and stress wave amplitude in sandstone under static stress," *Journal of Yangtze River Scientific Research Institute*, vol. 35, no. 10, pp. 115–119, 2018.

[13] W. Lu, J. Yang, P. Yan et al., "Dynamic response of rock mass induced by the transient release of in-situ stress," *International Journal of Rock Mechanics and Mining Sciences*, vol. 53, no. 7, pp. 129–141, 2012.

[14] Y. Cheng, X. X. Chang, C. He et al., "Analysis of stress wave characteristics of concrete pile based on analytic equation," *Journal of Jiangxi University of Science and Technology*, vol. 37, no. 5, pp. 41–46, 2016.

[15] J. Y. Xu, X. C. Lu, J. Zhang et al., "Research on energy properties of rock cyclical impact damage under confining pressure," *Chinese Journal of Rock Mechanics and Engineering*, vol. 29, no. 2, pp. 4159–4165, 2010.

[16] Y. Ju, L. Sudak, and H. Xie, "Study on stress wave propagation in fractured rocks with fractal joint surfaces," *International Journal of Solids and Structures*, vol. 44, no. 13, pp. 4256–4271, 2007.

[17] N. N. Li, J. C. Li, H. B. Li et al., "SHPB experiment on influence contact area of joints on propagation of stress wave," *Journal of Rock Mechanics and Engineering*, vol. 34, no. 10, pp. 1994–2000, 2015.

[18] S. H. Liu, D. B. Mao, Q. X. Qi, and F.-M. Li, "Under static loading stress wave propagation mechanism and energy dissipation in compound coal-rock," *Journal of China Coal Society*, vol. 39, no. 1, pp. 15–22, 2014.

[19] X. Guo and P. Wei, "Effects of initial stress on the reflection and transmission waves at the interface between two piezoelectric half spaces," *International Journal of Solids and Structures*, vol. 51, no. 21-22, pp. 3735–3751, 2014.

[20] E. D. H. Davies and S. C. Hunter, "The dynamic compression testing of solids by the method of the split Hopkinson pressure bar," *Journal of the Mechanics and Physics of Solids*, vol. 11, no. 3, pp. 155–179, 1963.

[21] X. B. Li, T. S. Lok, and J. Zhao, "Dynamic characteristics of granite subjected to intermediate loading rate," *Rock Mechanics and Rock Engineering*, vol. 38, no. 1, pp. 21–39, 2005.

[22] J. F. Jin, X. B. Li, T. B. Yin et al., "Effect of axial static stress of elastic bar on incident stress wave under axial impact loading," *Engineering Mechanics*, vol. 30, no. 11, pp. 21–27, 2013.

[23] G. S. Wang, C. H. Li, S. L. Hu et al., "A study of time-and spatial-attenuation of stress wave amplitude in rock mass," *Rock and Soil Mechanics*, vol. 31, no. 11, pp. 3485–3492, 2010.

[24] X. L. Liu, J. H. Cui, X. B. Li et al., "Study on attenuation characteristics of elastic wave in different types of rocks," *Chinese Journal of Rock Mechanics and Engineering*, vol. 31, no. 1, pp. 3223–3230, 2018.